

Critical inertia for particle capture is determined by surface geometry at forward stagnation point

Joshua F. Robinson,^{1,2,3,*} Patrick B. Warren,^{1,4,†} Matthew R. Turner,^{5,‡} and Richard P. Sear^{5,§}

¹STFC Hartree Centre, Sci-Tech Daresbury, Warrington, WA4 4AD, United Kingdom

²H. H. Wills Physics Laboratory, University of Bristol, Bristol BS8 1TL, United Kingdom

³Institut für Physik, Johannes Gutenberg-Universität Mainz, Staudingerweg 7-9, 55128 Mainz, Germany

⁴SUPA and School of Physics and Astronomy, The University of Edinburgh, Peter Guthrie Tait Road, Edinburgh EH9 3FD, United Kingdom

⁵School of Mathematics and Physics, University of Surrey, Guildford, GU2 7XH, United Kingdom

(Dated: February 26, 2025)

Aerosols are ubiquitous, and particle capture from particle-laden air as it flows past an obstacle is of widespread practical importance. Neglecting diffusion, previous work has shown that for a smooth curved surface in both Stokes flow and inviscid flow, only particles with inertia above a threshold value (quantified by the nondimensional Stokes number) collide with the surface. Here we show that the critical Stokes number decreases with increasing Reynolds number of the air flow, and the mechanism behind this threshold is the same at all finite Reynolds numbers but becomes qualitatively different in the limit of infinite Reynolds number (inviscid flow). In addition we show that in the latter case (inviscid flow) the threshold is set solely by the flow near the stagnation point, whereas at finite Reynolds numbers the threshold also depends on the flow far from the stagnation point. The threshold also depends on obstacle geometry and we show that fibers whose cross section is flattened along the flow direction have greater size selectivity than fibers with a circular cross section.

I. INTRODUCTION

The air we breath is an aerosol; it contains suspended particles, with sizes up to tens of micrometres. When air flows around an obstacle, aerosol particles may collide with and so deposit on, the obstacle. This can cause problems, such as freezing water droplets causing the icing of aircraft wings and wind turbine blades [1–3]. It can also be useful, face masks and other air filters rely on aerosol particles depositing on their (typically $\sim 10 \mu\text{m}$) fibers [4–9] to remove these aerosol particles from the air. Other applications include aerosolised drugs [10], the wind-pollination of plants (anemophily) [11], and the harvesting of water from fogs by plants and animals [12], and by humans [13]. There are also industrial [14] and geological applications [15]. The same physics also occurs when particles suspended in a flowing liquid, such as sea water, deposit on an obstacle, for example, as happens with coral feeding on plankton [16]. It is worth noting that these varied flows cover the complete range of Reynolds numbers. In air filters it is much less than one, i.e. we have Stokes flow. With aircraft wings and wind turbine blades though, the Reynolds number is typically much larger (not least because the length scale is enormously bigger).

Here we study collisions of a particle with an obstacle, or ‘collector’, when the collisions are driven by the inertia of the aerosol particle, which causes it to deviate from the streamlines of the air flow. These streamlines flow around the obstacle so a point particle that follows streamlines perfectly always goes around an obstacle having without colliding with it. Particles with inertia do not follow the streamlines, meaning they can collide with an obstacle’s surface. In 1931, Albrecht [17] found

a threshold in the inertia, below which no (point) particles deposited on the obstacle. A minimum amount of inertia is needed before any (point) particles are deposited. Then in the 1940s, first Taylor [1], and then Langmuir and Blodgett [2] calculated this critical value of the inertia. The particle inertia is characterised by the Stokes number, St , and the threshold is at some critical value $St = St_c$.

There has been considerable work on this problem since the works of Taylor [1], Langmuir and Blodgett [2] in the 1940s [18, 19], motivated by its many applications. How the threshold varies with Reynolds number has been studied by Phillips and Kaye [20], and Araújo *et al.* [21] computed the deposition efficiency on cylinders in low Reynolds number flow. They found that the critical scaling for the deposition efficiency was $\lambda \propto (St - St_c)^{1/2}$. Vallée *et al.* [22] studied deposition on spheres, using analytics and computationally. They determined both the critical value of the Stokes number as a function of the Reynolds number of the flowing air, and the critical scaling of the deposition efficiency. At low Reynolds number they showed that the critical scaling is $\lambda \propto (St - St_c)^1$. Deposition occurs on a line for Araújo *et al.*’s cylinders and on an area for Vallée *et al.*’s spheres, so the exponent found by Vallée *et al.* [22] should be, and is, twice that found by Araújo *et al.* [21]. As Vallée *et al.* [22] first showed, the critical scaling is very different for inviscid (high Reynolds number) flow around a sphere. The scaling is not a power law but the unusual behaviour $\lambda \propto \exp(-1/(St - St_c)^{1/2})$. This also applies for a cylinder [23].

Here we characterise the dynamical transition that sets the critical deposition threshold at $St = St_c$, and show how it is determined by the flow field near the forward stagnation point at the front of the obstacle. This stagnation point (e.g. the white circle in Fig. 2a) is a point where the flow velocity is zero and where the flow divides to go around the obstacle. We also show why, just above the threshold, the amount of aerosol deposition scales as $(St - St_c)^{1/2}$, for air flow at finite Reynolds numbers, Re , but not for inviscid ($Re \rightarrow \infty$) flow. It

* joshua.robinson@stfc.ac.uk

† patrick.warren@stfc.ac.uk

‡ m.turner@surrey.ac.uk

§ r.sear@surrey.ac.uk; <https://richardsear.me/>

is important to understand aerosol deposition as a function of Reynolds number as in applications Re varies from less than one (masks) to millions (aircraft wings).

Defining a Stokes number requires a length scale from the (air flow round the) obstacle. For a long cylinder normal to the flow there is only one length scale, the radius R , see Fig. 1a, and this sets the local curvature at the stagnation point. To better understand how to control the critical Stokes number and collection efficiency of an obstacle, we generalise from a circular cross-section to an elliptical cross-section, see Fig. 1b.

Ellipses, like discs, are smooth curved bodies, and there are well known analytic expressions for inviscid flow around ellipses using conformal mapping techniques [24]. Unlike a disc, which has just one length scale, ellipses have two. These can be of a few different pairs, one example pair is the half-length along the flow direction, $\hat{\ell}_x$, and half-length normal to that direction, $\hat{\ell}_y$, as in Fig. 1b. Here we only consider ellipses with a symmetry axis (semi-major or semi-minor) along the flow direction.

Most of the work for high Reynolds numbers has been computational or theoretical, as experiments on collisions in these flows are challenging. However, Wong and coworkers did obtain some experimental data on deposition efficiency at Reynolds numbers of a few hundreds [25]. This was for an aerosol with particles with a narrow distribution of sizes. They found no measurable deposition below a threshold near that predicted by Taylor [1], and by Langmuir and Blodgett [2]. So these experiments agree with theoretical predictions (for a simplified model) that a threshold exists. Makkonen and coworkers [26] have measured ice deposition on cylinders. This is for the typical case in the environment, where the droplets have a broad range of sizes, which complicates comparison with theoretical predictions.

In section II we present our model for inertial particles impacting on elliptical obstacles. We then analyse how critical inertia emerges in two distinct limits in section III. In section IV we examine how the efficiency of particle capture varies above the critical threshold in each limit, and how this is affected by elliptical eccentricity. Last, in section V we discuss some recent work where the critical inertia can be calculated analytically, before concluding with some perspectives on filters. All calculations underlying this work are available in Ref. [27].

II. MODEL

Here we consider a simple model: point particles that interact with the obstacle only when they collide. Real particles have a size and exhibit more realistic interactions with the obstacle (e.g. electrostatics in masks made to N95/FFP2 standards [4]). However, aerosol particles are typically no more than tens of micrometres in size and in some cases the obstacle can be tens of centimetres across, so the particles are much smaller than the obstacle and thinking of them as point particles is a good approximation. For air filters (including masks) the obstacle diameter is much smaller and can be comparable to the particle size. Here particle size does affect deposition [4, 7, 9] but the dynamical transitions we study here may well

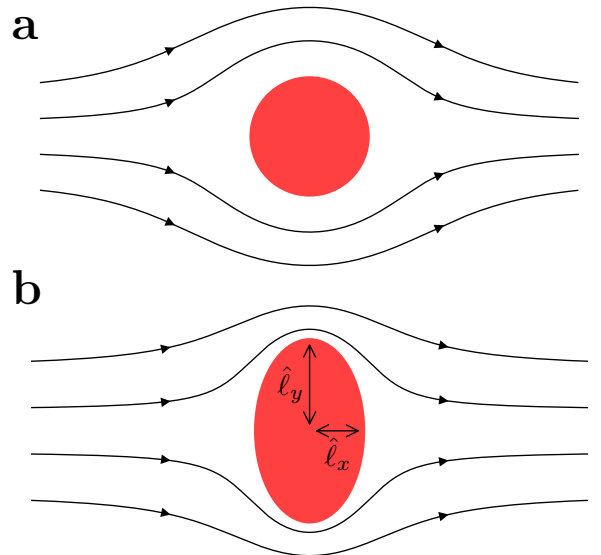


FIG. 1. (colour online) Fluid flows around cylindrical collectors with (a) circular and (b) elliptical cross-sections. These collectors represent idealised obstacles in filters.

underlie some counterintuitive behaviour seen for particles with a non-zero diameter: Under some circumstances, increasing particle inertia *decreases* the amount of deposition [7, 9, 28].

We study a simple model of point particles depositing onto bodies that are infinite along the z axis and either circular or elliptical in the $x - y$ plane. So our problem is two dimensional. The ellipses are orientated perpendicular to the flow as shown in Fig. 1b.

As Taylor [1], and Langmuir and Blodgett [2] realised, particle capture occurs within a stagnation point flow. Stagnation points are loci where the flow velocity is zero. Every point along a surface where a no-slip boundary condition is applied in viscous fluid flow could be considered as a stagnation point, but for our purposes we only use “stagnation point” to refer to such points where the flow speed would be zero regardless of boundary condition. Ellipses have stagnation points at the mid-point of their surface where the flow is bisected. See the horizontal streamlines in Fig. 2a for the case of a cylinder.

For a particle suspended in flowing air we assume that the only force on the particle is the friction with the surrounding air, which is taken to be proportional to the difference between particle’s velocity $\hat{\mathbf{v}}$ and the local flow velocity $\hat{\mathbf{u}}$. This force is taken to act on the particle’s centre of mass. Then Newton’s equation for the particle motion is

$$m \frac{d\hat{\mathbf{v}}}{d\hat{t}} = -\xi(\hat{\mathbf{v}} - \hat{\mathbf{u}}) \quad (1)$$

for a particle of mass m and with drag coefficient ξ . We use a hat ($\hat{}$) to indicate a dimensional quantity. We shall also need a characteristic flow speed U , which is discussed further below. We switch to nondimensional quantities via transformations $\mathbf{r} = \hat{\mathbf{r}}/\hat{\ell}_y$, $\mathbf{u} = \hat{\mathbf{u}}/U$ and $t = U\hat{t}/\hat{\ell}_y$ where $2\hat{\ell}_y$ is the cross-sectional width of the ellipse in the plane transverse to the

incoming flow, see Fig. 1. This leads to

$$\text{St} \dot{\mathbf{v}} + \mathbf{v} - \mathbf{u} \equiv \text{St} \ddot{\mathbf{r}} + \dot{\mathbf{r}} - \mathbf{u} = 0, \quad (2)$$

where $\text{St} = mU/(\hat{\ell}_y \xi)$ is the Stokes number giving the effective inertia, and the dot ($\dot{}$) indicates derivative with respect to nondimensional time t . In our dimensionless units we have effective ellipse dimensions $\ell_x = \hat{\ell}_x/\hat{\ell}_y$ and $\ell_y = \hat{\ell}_y/\hat{\ell}_y \equiv 1$. The circular case is recovered by setting $\ell_x = 1$ in these units.

We are interested in particle trajectories that pass close to the forward stagnation point. We take the origin to be at the centre of the obstacle so that this stagnation point occurs at $(r, \theta) = (\ell_x, \pi)$ in polar coordinates. In polar coordinates we must include inertial terms in the acceleration term of Eq. (2). Decomposing $\mathbf{u} = u_r \mathbf{e}_r + u_\theta \mathbf{e}_\theta$ where \mathbf{e}_r and \mathbf{e}_θ are unit vectors in the radial and azimuthal directions respectively, we find

$$\begin{aligned} \text{St}(\ddot{r} - r\dot{\theta}^2) &= -(\dot{r} - u_r), \\ \text{St}(r\ddot{\theta} + 2\dot{r}\dot{\theta}) &= -(r\dot{\theta} - u_\theta). \end{aligned} \quad (3)$$

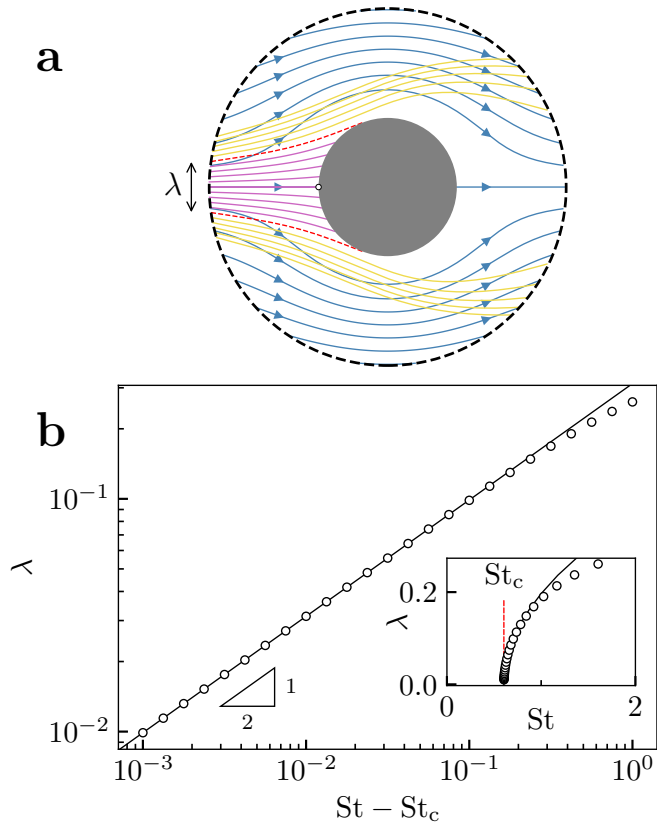


FIG. 2. (colour online) Particle capture by a cylindrical collector at zero Reynolds number flow (via the Kuwabara flow field with volume fraction $\alpha = 0.15$). (a) Representative trajectories at $\text{St} = 2$ in the Kuwabara flow field (light blue) which hit (purple) or miss (yellow) the cylindrical collector (grey). Trajectories are launched with zero initial acceleration from the outer circular perimeter of the Kuwabara flow field where the vorticity vanishes (dashed). The forward stagnation point is shown with a white circle. (b) Capture efficiency λ as a function of Stokes number St ; the points are from numerical experiments and the solid line is $\lambda \propto \sqrt{\text{St} - \text{St}_c}$ with $\text{St}_c \simeq 0.604$.

For the the original Eqs. (1) there is often a natural choice of U for any given problem, e.g. the flow speed infinitely far from a cylinder U_∞ . Fernandez de la Mora and Rosner [28] have pointed out that alternative choices of U can be made, giving different Stokes numbers for the same system. The particular choice selects a distinct different asymptotic regime of validity [29]. Following these authors [28], we take our characteristic flow speed to be the magnitude of the *local* flow approaching the stagnation point. With this choice the normal component of flow expands about the stagnation point as

$$u_r = -(r - \ell_x)^m + o\left((r - \ell_x)^m\right)$$

as $r \rightarrow \ell_x$, with exponent $m > 0$ ensuring no penetration. Note in the case of inviscid flow around the circle/ellipse this choice involves taking $U = 2U_\infty$, so our Stokes number will be double that of authors taking $U = U_\infty$.

III. ON-AXIS FLOWS AND THE CRITICAL STOKES NUMBER

As Taylor [1], and Langmuir and Blodgett [2] realised, there is a threshold inertia, and so Stokes number, below which no point particles collide with an obstacle. The particles all follow the fluid flow around the obstacle. This threshold or critical Stokes number, St_c , depends only on the on-axis flow (i.e. with constant $\theta = \pi$) [1, 2, 22]. In this section we will compute values for St_c .

A. On-axis flow fields and equations of particle motion

On-axis ($\theta = \pi$) the particle equation of motion reduces to a single differential equation for $r(t)$. It is convenient to introduce the auxiliary variable $x = r - \ell_x \in [0, \infty)$ quantifying the distance from the forward stagnation point. Below the critical Stokes number St_c there are no collisions in finite time. The on-axis particle will eventually reach the surface at $x = 0$ but only in the limit $t \rightarrow \infty$. By contrast, the particle reaches $x = 0$ in finite time for $\text{St} > \text{St}_c$ which we call a collision.

On-axis, the equation of motion Eq. (3) reduces to

$$\text{St} \ddot{x} = -(\dot{x} - u_r). \quad (4)$$

We consider three possible on-axis flow fields u_r

$$u_r(x) = \begin{cases} -x^2 & \text{incompressible Stokes flow} \\ -x & \text{inviscid flow} \\ -x^m & \text{generalised flow} \end{cases}. \quad (5)$$

Note that the proportionality constant is unity in each case from our choice of U in the definition of St (see end of previous section).

The quadratic scaling of the first flow field $u_r \propto -x^2$ is generic to incompressible flows where a no-slip boundary condition is applied. The specific case we will consider is the leading order term in a small x expansion in the vicinity of

the stagnation point for Stokes flow around a cylinder. The so-called ‘‘Stokes paradox’’ [30] prohibits Stokes flows around isolated cylinders [31], so the underlying flow field must be imagined as a finite pore in a dense media. As a specific flow field we take the Kuwabara flow which was developed to approximate an array of equally spaced cylinders [32]. Note that the constant of proportionality in this case depends (weakly) on the density of cylinders. The Kuwabara flow field and its expansion is given in section 1 of the Supplemental Material (SM).

The second flow field is the leading order term for inviscid flow near a stagnation point on the surface of an ellipse. More generally, a linear leading flow is expected wherever incompressibility or the no-slip boundary condition is relaxed. The flow field for inviscid flow past an ellipse is given in section 3 of the SM. The final flow field with $m \in [1, 2]$ is a generalised near-stagnation-point flow field, which we use to continuously vary the limiting flow past a cylinder between the inviscid limit at $m = 1$ and the Stokes limit at $m = 2$.

B. Incompressible Stokes flow

For Stokes flow impinging on a cylinder we have the Stokes flow field of Eq. (5), which when inserted into Eq. (4) gives

$$\text{St} \ddot{x} + \dot{x} + x^2 = 0 \quad \text{incompressible Stokes flow} \quad (6)$$

We start by setting $\text{St} = 1$. By following trajectories at differing initial conditions we can plot phase portraits in the $x - \dot{x}$ plane, see Fig. 3a. Valleé *et al.* [22] have obtained essentially the same phase portrait (the left panel of their Fig. 8). There are two kinds of trajectories: The first kind (shown in yellow) asymptotically approach the marginally-stable fixed point at $x = \dot{x} = 0$. They therefore do not collide with the surface in finite time. The second kind (purple) reach $x = 0$ in finite time and with $\dot{x} < 0$, and so collide with the surface. The two kinds of trajectories lie in attractor basins for, respectively, the fixed point at the origin (yellow), and a second attractor located at ‘ $-\infty$ ’ in x and $u = \dot{x}$ (purple). This second attractor is inaccessible here due to collisions at $x = 0$.

Now that we know there are two attractor basins, we ask how this phase-space geometry is affected by changing St . Increasing St in Fig. 3b we see the noncolliding basin contracts as more initial collisions result in collisions. This explains the threshold in inertia needed to see collisions: keeping the initial condition fixed, increasing St will transition the resulting trajectory from a noncolliding state to a colliding state when the basin shrinks away from the selected state. This transition is discontinuous, but the time to collision diverges.

Despite the fact that we have plotted two phase portraits for the Stokes-flow case, there is in fact only one phase-portrait topology at all values of St . The Stokes number St can be eliminated from Eq. (6) with the change of variables $x(t) = \tilde{x}(\tau)/\text{St}$ and $\tau = t/\text{St}$ so that $\partial_t = \text{St}^{-1} \partial_\tau$. Now we have

$$\partial_\tau^2 \tilde{x} + \partial_\tau \tilde{x} + \tilde{x}^2 = 0. \quad (7)$$

This has yielded a universal equation for on-axis particles in incompressible stagnation point flows subject to a no-slip

boundary condition. Thus in the $\tilde{x}-\tilde{x}_\tau$ plane there is only one universal phase portrait, with one global topology. Changing the value of, for example St , cannot change the phase portrait topology. Note that in the generalised flow case the rescaling $x(t) = \tilde{x}(\tau)/\text{St}^{1/(m-1)}$ with τ above for $m \neq 1$ gives the same universal phase-portrait with respect to St for Eq. (4); the phase portraits shown in Fig. 3e–f for noninteger values of m are also universal in this sense.

As the critical inertial value depends on the initial condition, the identification of a critical Stokes number depends on the relationship between $x(t=0)$ and $\dot{x}(t=0)$. The most natural initial condition is for a particle to be dropped into the flow with zero initial acceleration $\ddot{x} = 0$, i.e. along the nullcline of the fluid flow velocity. We have plotted the velocity nullcline as the dashed curve in Fig. 3a–c. The critical value of $x(t=0; \text{St})$ then occurs where this nullcline intersects the colliding basin for the first time when moving out from the origin. For $\text{St} = 1$, we numerically find a critical initial condition of $x_c(t=0) \simeq 0.597$ by following trajectories backwards in time from the origin along the separatrix and observing where this intersects the nullcline.

Finally, we note that our rendered phase portraits were obtained using a small x expansion. We have performed similar calculations using a more complete flow field (the Kuwabara flow) which resulted in the same basic phase portraits and a threshold inertia. As such, we believe the phase space geometry described above is universal for stagnation point flows at smooth obstacles with the no-slip boundary condition applied.

C. Inviscid flow

Here the stagnation point is very different to that in Stokes flow, the flow velocity varies linearly not quadratically with distance from the stagnation point [23, 24]. We then have the equation of simple harmonic motion (SHM), as many others have realised [1, 2, 22]. It is a classic physical problem to show that SHM permits two classes of solution: exponentially decaying solutions (overdamped) for $\text{St} < \frac{1}{4}$ and periodic solutions (underdamped) for $\text{St} > \frac{1}{4}$. These are in Fig. 3c–d. The overdamped solutions only collide as $t \rightarrow \infty$ while the underdamped solutions collide in finite time. So here the critical Stokes number $\text{St}_c = 1/4$ for a cylinder. This was first realised by Taylor [1], and by Langmuir and Blodgett [2]. Note they actually quote $\text{St}_c = 1/8$ which differs by a factor of 2 because of their alternative choice to set $U = U_\infty$ (see discussion at end of section II).

At St_c there is a *global* topology change in the phase portrait in the inviscid case, compare Fig. 3c and d. For $\text{St} > \text{St}_c$ all trajectories collide (are underdamped in SHM language).

D. Different mechanisms for critical Stokes numbers in the Stokes-flow and inviscid-flow limits

We can see from the phase portraits in Fig. 3 that there are two completely different mechanisms for generating a critical Stokes number describing a dynamical transition. For inviscid

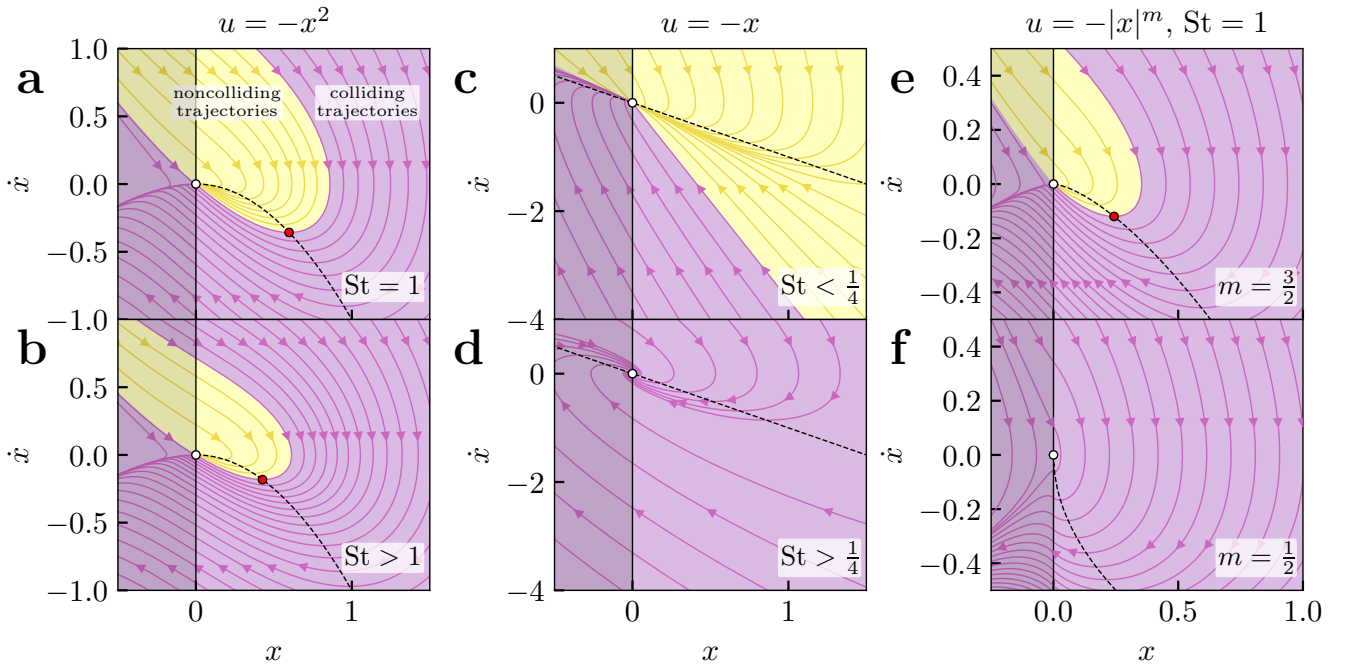


FIG. 3. (colour online) Phase space portraits for the on-axis problem in the (x, \dot{x}) -plane for (a-b) Stokes flow, (c-d) inviscid flow, and (e-f) more general power law flows (noninteger m). (a) to (b), and (c) to (d), the Stokes number is increased, while from (e) to (f) the exponent m increases at fixed Stokes number. In all panels, trajectories that collide are shown in yellow, while trajectories that do not collide (except at $t \rightarrow \infty$) are in purple. The dashed curves are velocity nullclines, where $\ddot{x} = 0$, which provides a natural initial condition at any x . The critical initial conditions $x_c(t=0)$ leading to collisions are also shown (red points) for the Stokes flows in (a-b), and in (e); there is no such dependence on initial conditions in the inviscid case.

flow $St_c = 1/4$, a universal value is set by the stagnation-point flow alone, and St_c is set by a change in topology of the phase portrait, going from Fig. 3c to d [33]. In this case, perturbing the flow field far from the stagnation point does not change the value of St_c . So in practice we expect that at high Reynolds number perturbing the global flow field far from the stagnation point should only very weakly alter the value of St_c .

However for Stokes flow, the value of St_c depends on the initial conditions, and there is only one phase portrait topology (i.e. that of Fig. 3a). A consequence of this is that the numerical value of St_c will depend on the full flow field, not just the limiting flow at the stagnation point. For example, perturbing the flow upstream by adding another cylinder would change the value of St_c .

In Fig. 4b we show results for the value of St_c as a function of the exponent m in the distance dependence of the flow speed near the stagnation point. We see that only for $m = 1$ is there a universal value of St_c . For larger values, $m > 1$, there is a critical value of the Stokes number, but it will depend on the flow field far from the stagnation point. So the value $m = 1$ is the special case, as in Fig. 3. When $m < 1$ there are collisions at all values of the Stokes number and so no critical value.

E. Hiemenz flows for large but finite Reynolds numbers

We have seen that the inviscid, infinite Reynolds number, case is a special case. To obtain some insight into the behaviour at large but finite Re we use the Hiemenz flow field [34, 35]. This flow field is a simple model for flow at large Re near a stagnation point on a plane (so we cannot consider the effects of curvature). The Hiemenz flow [34] models stagnation point flows *exactly*, albeit only asymptotically close to the dividing flow. This flow features two parts: An inner part, the boundary layer, where the flow is akin to Stokes flow satisfying the no-slip boundary condition, and an outer part, where it is close to inviscid flow [24]. The boundary layer has a thickness that scales as $Re^{-1/2}$, and so this thickness tends to zero as the Reynolds number increases. See SM for details of this flow field.

We show the critical Stokes number St_c as a function of Reynolds number Re in Fig. 4a. Just as in the power law case, we recover the universal inviscid limit, and we see that as we move away from this, the critical Stokes number depends on the initial condition. Thus we expect that St_c is only set by the stagnation point flow in the limit of inviscid flow, but that at large Reynolds number, the dependence of the value of St_c on the flow field far from the stagnation point becomes weak.

As an example of Stokes flow, we also show St_c for the Kuwabara approximate flow of one cylinder in an array of cylinders. We studied this system in an earlier work [9]. The

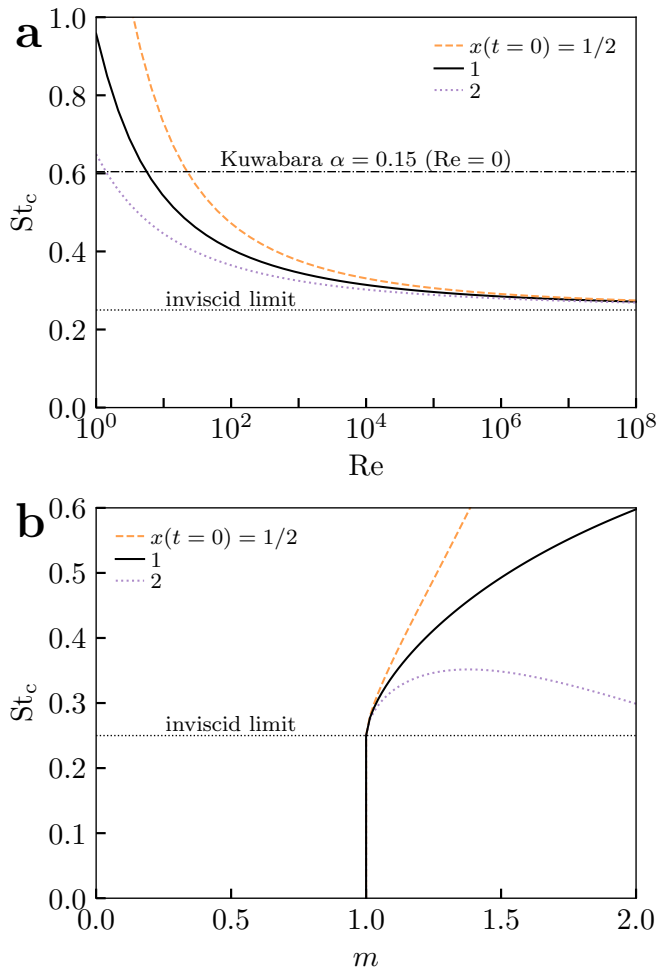


FIG. 4. (colour online) Critical Stokes numbers above which collision occurs on-axis $y = 0$ for different initial conditions. (a) Stagnation point flows (Hiemenz flow) at finite Reynolds number Re . (b) Power law flows $\mathbf{u} \propto (-|x|^m, m|x|^{m-1}y)^\top$, transitioning from Stokes to inviscid flows as m decreases from 2 to 1. These both trend towards the inviscid limit $St_c = 1/4$ (dotted line) as $Re \rightarrow \infty$ or $m \rightarrow 1$.

value of St_c depends on the density α of the array.

F. Ellipses in inviscid flow

Finally we consider ellipses in inviscid flow, see Fig. 1. The flow field near the stagnation point simply changes from $-x$ for a cylinder to $-\frac{1}{2}(1 + \ell_x)x$ for an ellipse (see section 3 of the SM). For inviscid flow the flow near the stagnation point sets the value of St_c . So for an ellipse in inviscid flow the critical Stokes number is simply

$$St_c = \frac{1}{2(1 + \ell_x)}. \quad (8)$$

When $\ell_x = 1$ we recover $St_c = 1/4$ for a cylinder. The $\ell_x = 0$ limit of the ellipse is a thin chord (wall) perpendicular to the flow, of length 2 in our non-dimensional units, and here $St_c = 1/2$, twice that for a cylinder. In the large ℓ_x limit the

ellipse becomes very elongated along the flow direction, and the critical Stokes number decreases as $1/\ell_x$. Eq. (8) is compared to numerical results in Fig. 5. The agreement is excellent.

IV. INERTIA-DRIVEN COLLISIONS OFF AXIS

We now turn to particles approaching off axis ($\theta \neq \pi$). Here we are interested in the width of the collection window λ , within which particles collide with the obstacle and outside which they circumvent it. The width λ is illustrated in Fig. 2a, as the distance between the limiting (dashed red) trajectories that just collide. This width gives an estimate of the collection efficiency.

For limiting off-axis flows about the forward stagnation point, it is convenient to introduce a second variable $y = \ell_x(\theta - \pi)$ quantifying the azimuthal distance from the stagnation point. In this section we focus on flows with circular symmetry $\ell_x = 1$ in the asymptotic limit approaching the forward stagnation point. The particle equation of motion Eq. (3) becomes

$$\begin{aligned} St(\ddot{x} - (1+x)\dot{y}^2) &= -(\dot{x} - u_r), \\ St\left(\ddot{y} + \frac{2}{1+x}\dot{x}\dot{y}\right) &= -\left(\dot{y} - \frac{u_\theta}{1+x}\right). \end{aligned}$$

Expanding around the stagnation point and discarding terms beyond leading order, we find this reduces to

$$\begin{aligned} St(\ddot{x} - y^2) &= -(\dot{x} - u_r), \\ St(\ddot{y} + 2\dot{x}\dot{y}) &= -(\dot{y} - u_\theta). \end{aligned} \quad (9)$$

approaching the stagnation point. For the remainder of this section we will consider particle trajectories following Eq. (9) using limiting flows we introduced in the previous section. We will return to ellipses using the full (non-expanded) equation of motion Eq. (3) in the next section.

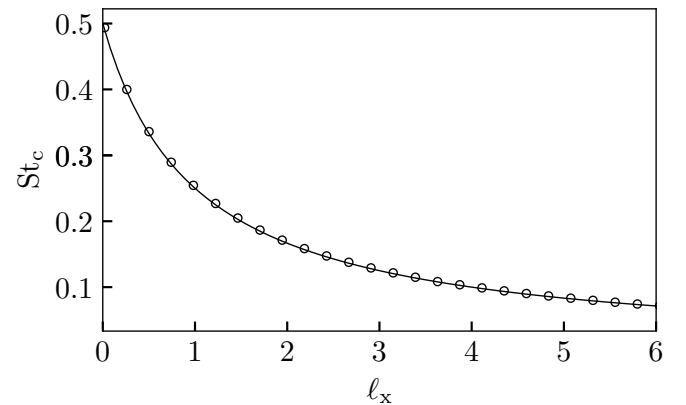


FIG. 5. (colour online) The critical Stokes number for an ellipse in inviscid flow, as a function of the length of the ellipse along the flow direction. The length of the ellipse perpendicular to the flow direction is kept constant and is the length scale used to define the Stokes number. The points are the results of numerical calculations, and the curve is Eq. (8). The initial conditions taken were $r(0) = 10$, $\theta(0) = \pi$, $\dot{r} = u_r$ and $\dot{\theta} = 0$ and full flow field (not Eq. (5)) is used.

For our chosen flows we determine the critical Stokes number St_c and the efficiency λ numerically via an iterative procedure. For a given initial condition, we assign a trial Stokes number St to the midpoint between the lower and upper bounds for St_c and follow the trajectory to test for a collision. We update either the lower or upper bounds for St_c depending on whether collision occurs. Each iteration therefore provides approximately 1 bit of information, which converges to sufficient precision for our plots after 20 iterations. Once we have St_c we obtain $\lambda(St)$ via a very similar procedure: for each $St - St_c$ we vary $y(t=0)$ to adjust the best upper/lower bounds for λ at this value of St . We always assume the initial condition $x(t=0) = 1$ and $\dot{x}(t=0) = 0$.

A. Flow fields near stagnation points and the resulting equations for particle motion

Here we use the Kuwabara flow field [32] for flow around a cylinder in an array of cylinders representing e.g. porous media. The area of this cylindrical pore is finite thus avoiding the Stokes paradox. The full flow field is given by Eq. (S1) in the SM. Expanding the flow field around the stagnation point gives the limiting flow

$$\mathbf{u} \propto (-x^2, 2xy)^T. \quad \text{Stokes, cylinder} \quad (10)$$

Due to the no-slip boundary conditions the flow speed tends to zero proportional to x^2 . The stagnation point is shown as a circle in Fig. 2a.

We now consider incompressible flow in two dimensions near a more general stagnation point. By ‘near’ we mean that the distance to the stagnation point is much smaller than any other length scale in the system (e.g. the size of the obstacle or distance to another obstacle). In this case, when all other length scales can be discarded, we expect the flow field to have power law behaviour. We write the resulting on-axis flow as $u_r \propto -x^m$, where the exponent $m \in [1, 2]$ so as to provide a transition from the inviscid flow case ($m = 1$) to the Stokes flow case ($m = 2$).

In two dimensions, the local incompressibility condition about the stagnation point in our (x, y) coordinates amounts to

$$\partial_x u_r = -\partial_y u_\theta. \quad (11)$$

The flows bifurcate at the stagnation point, so u_θ can only involve odd powers of y , with the leading term being linear $u_\theta \propto y$. But now that we have u_r , incompressibility Eq. (11) gives us $u_\theta \propto -mx^{m-1}y$ with the same constant of proportionality as for u_r . Combining the two components, the limiting flow field becomes

$$\mathbf{u} \propto (-x^m, mx^{m-1}y)^T \quad m > 0 \quad \text{general} \quad (12)$$

which is therefore generally expected near the stagnation point, for incompressible two-dimensional stagnation point flows. Far from the stagnation point the flow field must relax to some background flow.

Stagnation points of the general form of Eq. (12) are found on a range of bodies in flowing fluids, with m depending both

on the geometry of the body and on the Reynolds number. For a cylinder we have $m = 2$ for Stokes flow and $m = 1$ for inviscid flow. Flat walls belong to the same class as cylinders as they are obtained in the limit of infinite radius. Similarly, any smooth convex body, such as an ellipse, belongs to this class as its local geometry will be indistinguishable from that of a cylinder with a finite radius of curvature. Thus, for example, we expect qualitatively the same behaviour for ellipses as for discs, but note that, as we can see from the factors of ℓ_x in Eq. (S13) of the SM, details such as the value of critical Stokes number will change.

B. Limiting power-law flows

Here we present numerical data for the limiting power law flows $u = -|x|^m$ that we explored qualitatively (with phase portraits) in the previous section and in Fig. 3. Recall that $m = 2$ corresponds to a no-slip boundary condition (limiting Stokes flow), and $m = 1$ to a slip boundary condition (limiting inviscid flow), so non-integer values of m interpolate these two limits.

We show how collection efficiency scales with $\delta = St - St_c$ in Fig. 6b for $m \in [1, 2]$. We find that for small δ and $m > 1$, the collection efficiency obeys the relation

$$\lambda \propto \delta^{1/2}. \quad (13)$$

This is exactly the exponent of one half that Araújo *et al.* [21] estimated computationally for Stokes ($Re = 0$) flow. There is a simple argument for why we should expect $\lambda \propto \delta^{1/2}$. This scaling is equivalent to $\delta \propto \lambda^2$, which is generic to any system with a Taylor series expansion for $\delta(\lambda)$ around $\lambda = 0$, which has symmetry such that $\delta(\lambda) = \delta(-\lambda)$ (which eliminates the term linear in λ). The cylinder and wedge are symmetric around $y = 0$, so we have that symmetry. In other words, due to the symmetry around the stagnation point, we only require that a Taylor series for $\delta(\lambda)$ exist.

The function $\delta(\lambda)$ describes the surface of intersection between the colliding manifold and the selected initial conditions; the Taylor series (and the scaling $\lambda \sim \delta^{1/2}$) breakdown when this surface becomes singular. One important limit where this happens is towards inviscid flows as $Re \rightarrow \infty$. This inviscid case corresponds to $m = 1$ where slip occurs at the boundary for power law flows. Vallée *et al.* [22] and Turner and Sear [23] have found explicitly the leading order behaviour for inviscid flow is $\delta \propto 1/(\ln \lambda)^2$ (equivalent to $\lambda \sim \exp(-1/\delta^{1/2})$); this scaling is reproduced in Fig. 6b for $m = 1$. This analytic form does not have a Taylor series expansion around $\lambda = 0$: the derivatives diverge. So the Taylor series breaks down as $Re \rightarrow \infty$, violating the assumption of our argument above.

The limiting power law flow $u = -|x|^m$ universally applies as we approach a stagnation point. It is perhaps surprising that the entire phenomenology of a normal square root scaling Eq. (13) (and its breakdown in the inviscid limit) is captured by such a simple limiting flow. To confirm the universality of this phenomenology we will next turn to more realistic flows at finite Reynolds number.

C. More realistic stagnation point flows

In order to confirm that the limiting flows display the general phenomenology of realistic flows, we now consider idealised stagnation point flows. In particular we consider the Stokes flow around a cylindrical collector in porous media (Kuwabara flow of Ref. [32]) and the stagnation point flow onto a plane at non-zero Reynolds number Re (Hiemenz flow of Ref. [34]). The Hiemenz flow [34] models stagnation point flows *exactly*, albeit only asymptotically close to the dividing flow. This flow features two parts: An inner part, the boundary layer, where the flow is akin to Stokes flow satisfying the no-slip boundary condition, and an outer part, where it is close to inviscid flow [24]. The boundary layer has a thickness that scales as $Re^{-1/2}$, and so this thickness tends to zero as the Reynolds number increases. See SM for details of this flow field. For the cylindrical Kuwabara flow we integrate the polar equations given in Eq. (3), and for the Hiemenz flow we integrate the equivalent equation in Cartesian coordinates.

This means the previously-obtained critical value of $St_c \approx 0.597$ is not a universal feature of Stokes flows. The threshold for capture in Stokes flow depends (weakly) on details of the flow geometry.

We show the efficiency of capture $\lambda(\delta)$ in Fig. 6a. As before in the simplified flows, we see a region of δ values over which we see a $\delta^{1/2}$ scaling, and the width of this region decreases with increasing Reynolds number. This is exactly what we would expect if a Taylor series expansion exists for particles in air flowing around a stagnation point in Stokes flow but *not* when the flow is inviscid. We have therefore reproduced the same phenomenology for these realistic flows as we obtained for the simplified power law flows, with breakdown of the $\delta^{1/2}$ scaling only occurring in the inviscid limit. This underscores the fact that the inviscid limit is truly singular, whereas other flows generically observe the critical efficiency scaling reported by Araújo *et al.* [21]

D. Ellipses in inviscid flow

Finally, we look at the effect of obstacle geometry on the collection efficiency λ . We do this by studying ellipses that are both elongated and flattened along the flow direction of inviscid flow. The collection efficiency as a function of Stokes number is plotted in Fig. 7. Results are plotted for both ellipses which are long along the flow direction, $\ell_x = 5$, and for ellipses flattened along the flow direction, $\ell_x = 0.2$.

As Vallée *et al.* [22] first showed for cylinders, for inviscid flow just above the St_c , λ has the unusual scaling $\lambda \propto \exp(-\delta^{-1/2})$. This is a much slower increase of λ than the $\delta^{1/2}$ dependence found in Stokes flow. In Fig. 7 we see that the unusual scaling $\lambda \propto \exp(-\delta^{-1/2})$ also holds for ellipses in inviscid flow.

The precise theoretical behaviour of the collection can be determined using the same analytical calculations laid out in

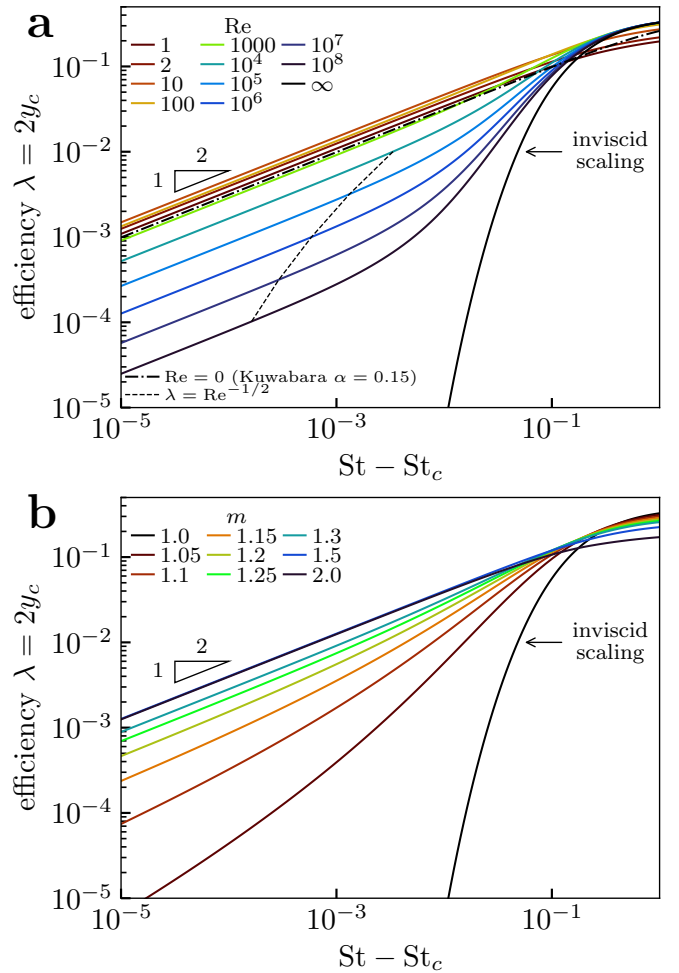


FIG. 6. (colour online) Critical scaling of collection efficiency λ above St_c with $x(t=0) = 1$. (a) Stagnation point flows at finite Reynolds number Re (Hiemenz flow). λ shows square root scaling for efficiencies smaller than the viscous boundary layer thickness $Re^{-1/2}$ (dashed line), and a cross-over to an inviscid-like scaling occurs at moderate Stokes numbers. This boundary layer vanishes as $Re \rightarrow \infty$ rendering the critical scaling singular. For reference, we also show the results for the realistic Kuwabara flow field (dash-dotted lines) in the limit $Re \rightarrow 0$ within porous media; this flow field seems to share similar properties to a Hiemenz flow with finite $Re = \mathcal{O}(1)$. (b) Power law flows $\mathbf{u} \propto (-|x|^m, m|x|^{m-1}y)^T$ captures the same phenomenology with a much simpler model. We observe square root scaling for small $St - St_c$ so long as $m > 1$, and we see a cross-over to an inviscid-like scaling at moderate Stokes numbers.

Section V of Turner and Sear [23] and we find that

$$\lambda \sim \exp\left(-\frac{(4 - \sqrt{2})}{4\sqrt{1 + \ell_x}}\pi\delta^{-1/2}\right), \quad (14)$$

The efficiency λ is predicted to increase more rapidly with St for ellipses oriented with their minor axis along the flow direction (small ℓ_x), than for ellipses oriented with their major axis along the flow direction.

From Fig. 5 we see that ellipses with small ℓ_x have large critical Stokes numbers, and from Fig. 7 we see that their

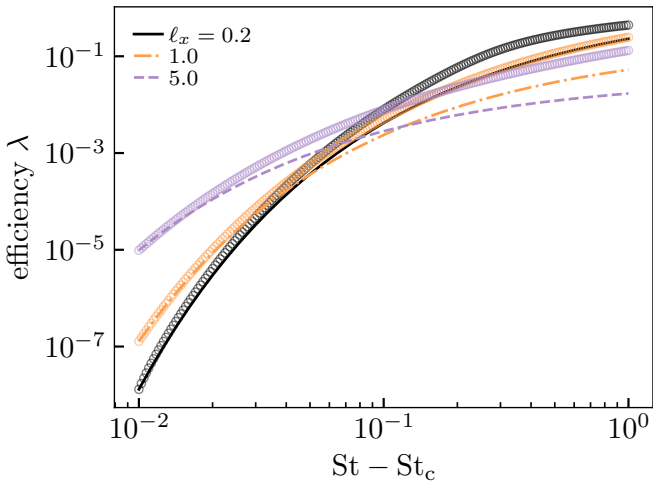


FIG. 7. (colour online) Collection efficiency λ as a function of Stokes number St , for ellipses with different aspect ratios. The points are results of the numerical integrations, while the lines represent the analytical result in Eq. (14).

collection efficiency increases rapidly above St_c . So ellipses (in high Reynolds number flows) with small ℓ_x look good candidates for size-selective filters for particles. The sharper increase of λ with St , and hence particle size, means they are more selective than cylinders.

V. RENORMALISATION-GROUP DERIVED SERIES EXPANSION RESULTS

The equation of the damped harmonic oscillator Eq. (2) is readily solvable by undergraduates with some training in ordinary differential equations (ODEs). By contrast, its deceptively simple extension to a quadratic restoring force (Eq. (4) with $m = 2$) or for general m requires a far more sophisticated treatment. In approaching these problems notice that the limit $St \rightarrow 0$ is singular in the sense that St multiplies the highest-order derivative in Eq. (2); the ODE is *qualitatively* different in the case $St \neq 0$ (where it is second-order) from $St = 0$ (where it is first-order). In addition, the time to reach the origin diverges as the critical trajectory is approached from the colliding manifold. It turns out that this diverging timescale can only be captured by perturbation theories which treat the singular behaviour of St .

A naïve perturbation theory constructed in powers of $St \ll 1$, which is only valid at short-times, therefore cannot capture the critical behaviour. In particular, secular terms in perturbation theory cause the solution to diverge in the long-time limit. Physically, this breakdown informs us that the relevant physics changes on different timescales. This is formally identical to how inertia comes to dominate viscosity at large Reynolds number and thus fluid flow physics changes with length scale [36]. Viscosity is important within a ‘boundary layer’ surrounding a surface, and unimportant far away. In our case, we have a *temporal* boundary layer: the flow field is unimportant within inertial timescales of $O(St^{-1})$, and on longer timescales of

$O(1)$ particles ‘forget’ their initial conditions and trace the flow field. Asymptotic methods were specifically developed to resolve this kind of problem.

In a forthcoming publication [37], two of us tease out the properties of the critical trajectory using the renormalisation group (RG) approach for solving singular differential equations [38]. We are able to derive a series expansion for the critical trajectory of the on-axis problem of Eq. (4) with $m = 2$, and our end result is the following series for the critical value [37]

$$(Stx)_c = 1 - \frac{1}{2} + \frac{1}{12} + \frac{1}{48} - \frac{1}{360} - \frac{17}{4320} - \frac{43}{80640} + \dots \quad (15)$$

Numerical tests [37] indicate the series is convergent, and the limiting value $(Stx)_c \simeq 0.597777$ agrees with the result found in Fig. 3a–b by numerical integrating trajectories. This work also demonstrates the usefulness of RG methods, which can readily handle the secular divergences at large times where standard perturbative methods fail.

VI. CONCLUSION

We have studied an aerosol flowing over a simple model obstacle (a cylinder), and determined how and when the inertia of the aerosol particles causes these particles to deposit onto the obstacle. For flow at all Reynolds numbers, there is a threshold amount of particle inertia below which no particles deposit. However, we have shown (see Fig. 3) that the dynamical transition that is behind this threshold is very different in the Stokes-flow and inviscid-flow limits.

In the inviscid limit, St_c is *only* a property of the stagnation point, while at any finite Reynolds numbers the threshold depends on the whole flow field, for example, in an array of cylinders, the threshold depends on the density of the array. Thus we expect the dependence of St_c on the flow field far from the stagnation point to be weak at large Re but significant for small Re .

Our calculations with Hiemenz flows suggests that St_c decreases with increasing Re . This matters for applications, as they span a huge range of Reynolds numbers from less than one for masks and other air filters [7, 9], to of order ten for beetles and small plants that harvest water from fog [12], to thousands to millions for wind-turbine blades [39] and aircraft wings.

For inviscid flow, St_c is set by the stagnation point flow and we have analytic expressions for the flow field around an ellipse. we used them to show that stretching a cylinder along the flow direction to form an ellipse with its major axis along the flow direction reduces the critical Stokes number. Thus ellipses with long axes along the flow direction should be able to filter out smaller particles, or particles at lower air speeds, at least if the flow Reynolds number is significant. Drag at high Reynolds is approximately proportional to the area normal to the flow [40], so elongating the ellipse along the flow direction increases the size range of particles filtered, without increasing the drag. So if an application requires maximum filtration with minimum drag, elliptical obstacles are superior to cylinders.

ACKNOWLEDGMENTS

Acknowledgements.—JFR and RPS wish to thank Paddy Royall for igniting our original interest in the complex problem

of particle capture during the early stages of the COVID-19 pandemic, and for many fruitful discussions. JFR acknowledges funding from the Alexander von Humboldt foundation. MRT acknowledges funding from the EPSRC via grants EP/W006545/1 and UKRI070.

-
- [1] G. I. Taylor, Notes on possible equipment and technique for experiments on icing on aircraft, Reports and Memoranda of the Aeronautical Research Committee **2024** (1940); *The Scientific Papers of Sir Geoffrey Ingram Taylor, vol 3: Aerodynamics and Mechanics of Projectiles and Explosions* (Cambridge University Press, Cambridge, UK, 1963).
- [2] I. I. Langmuir and K. Blodgett, *A Mathematical Investigation of Water Droplet Trajectories*, AAF Technical Report (Army Air Forces Headquarters, Air Technical Service Command, 1946).
- [3] O. Parent and A. Ilinca, Anti-icing and de-icing techniques for wind turbines: Critical review, *Cold Reg. Sci. Technol.* **65**, 88 (2011).
- [4] C.-S. Wang and Y. Otani, Removal of nanoparticles from gas streams by fibrous filters: A review, *Ind. Eng. Chem. Res.* **52**, 5 (2013).
- [5] J. Howard, A. Huang, Z. Li, Z. Tufekci, V. Zdimal, H.-M. van der Westhuizen, A. von Delft, A. Price, L. Fridman, L.-H. Tang, V. Tang, G. L. Watson, C. E. Bax, R. Shaikh, F. Questier, D. Hernandez, L. F. Chu, C. M. Ramirez, and A. W. Rimoin, An evidence review of face masks against COVID-19, *Proc. Natl Acad. Sci. USA* **118**, e2014564118 (2021).
- [6] T. Greenhalgh, M. B. Schmid, T. Czypionka, D. Bassler, and L. Gruer, Face masks for the public during the COVID-19 crisis, *BMJ*, m1435 (2020).
- [7] I. Rios de Anda, J. W. Wilkins, J. F. Robinson, C. P. Royall, and R. P. Sear, Modeling the filtration efficiency of a woven fabric: The role of multiple lengthscales, *Phys. Fluids* **34**, 033301 (2022).
- [8] J. F. Robinson, I. Rios de Anda, F. J. Moore, F. K. A. Gregson, J. P. Reid, L. Husain, R. P. Sear, and C. P. Royall, How effective are face coverings in reducing transmission of COVID-19?, *Aerosol Sci. Technol.* **56**, 473 (2022).
- [9] J. F. Robinson, I. Rios de Anda, F. J. Moore, J. P. Reid, R. P. Sear, and C. P. Royall, Efficacy of face coverings in reducing transmission of COVID-19: Calculations based on models of droplet capture, *Phys. Fluids* **33**, 043112 (2021).
- [10] W. H. Finlay, Aerosol physics and lung deposition modeling, in *Pharmaceutical Inhalation Aerosol Technology*, edited by A. J. Hickey and S. R. da Rocha (Taylor & Francis, Boca Raton, FL, 2019) 3rd ed., Chap. 4; C. Darquenne, Deposition mechanisms, *J. Aerosol Med. Pulm. Drug Deliv.* **33**, 181 (2020); E. Chalvatzaki, S. E. Chatoutsidou, and M. Lazaridis, Simulations of the deposition of pharmaceutical aerosols in the human respiratory tract by dry powder inhalers (DPIs), *J. Drug Deliv. Sci. Technol.* **59**, 101915 (2020); Y. S. Cheng, Mechanisms of pharmaceutical aerosol deposition in the respiratory tract, *AAPS PharmSciTech* **15**, 630 (2014); R. Zhang, Y. Li, A. L. Zhang, Y. Wang, and M. J. Molina, Identifying airborne transmission as the dominant route for the spread of COVID-19, *Proc. Natl Acad. Sci. USA* **117**, 14857 (2020).
- [11] K. T. Paw U and C. Hotton, Optimum pollen and female receptor size for anemophily, *Am. J. Botany* **76**, 445 (1989); K. J. Niklas, Wind pollination—a study in controlled chaos: Aerodynamic studies of wind-pollinated plants reveal a high degree of control in the apparently random process of pollen capture, *Am. Sci.* **73**, 462 (1985).
- [12] A. R. Parker and C. R. Lawrence, Water capture by a desert beetle, *Nature* **414**, 33 (2001); D. Mitchell, J. R. Henschel, R. S. Hetem, T. D. Wassenaar, W. M. Strauss, S. A. Hanrahan, and M. K. Seely, Fog and fauna of the Namib Desert: past and future, *Ecosphere* **11**, e02996 (2020); A. Shahrokhian, J. Feng, and H. King, Surface morphology enhances deposition efficiency in biomimetic, wind-driven fog collection, *J. Roy. Soc. Interface* **17**, 20200038 (2020).
- [13] M. Azeem, A. Guérin, T. Dumais, L. Caminos, R. E. Goldstein, A. I. Pesci, J. de Dios Rivera, M. J. Torres, J. Wiener, J. L. Campos, and J. Dumais, Optimal design of multilayer fog collectors, *ACS App. Mat. Int.* **12**, 7736 (2020).
- [14] A. Zamani and B. Maini, Flow of dispersed particles through porous media — Deep bed filtration, *J. Petrol. Sci. Eng.* **69**, 71 (2009).
- [15] T. F. Vasconcelos, A. D. Araújo, M. P. Almeida, and J. S. Andrade, Particle transport in rough channels, *Int. J. Mod. Phys. C* **20**, 1199 (2009).
- [16] M. Boudina, F. P. Gosselin, and S. Étienne, Direct interception or inertial impaction? A theoretical derivation of the efficiency power law for a simple and practical definition of capture modes, *Phys. Fluids* **32**, 123603 (2020); A. Espinosa-Gayosso, M. Ghisalberti, J. Shimeta, and G. N. Ivey, On predicting particle capture rates in aquatic ecosystems, *PLoS ONE* **16**, e0261400 (2021); M. R. Palmer, H. M. Nepf, T. J. R. Pettersson, and J. D. Ackerman, Observations of particle capture on a cylindrical collector: Implications for particle accumulation and removal in aquatic systems, *Limnol. Oceanogr.* **49**, 76 (2004).
- [17] F. Albrecht, Theoretische Untersuchungen über die Ablagerung von Staub aus strömender Luft und ihre Anwendung auf die Theorie Staubfilter, *Physik. Zeitschrift* **32**, 48 (1931).
- [18] K. J. Finstad, E. P. Lozowski, and E. M. Gates, A computational investigation of water droplet trajectories, *J. Atmos. Ocean. Technol.* **5**, 160 (1988).
- [19] K. J. Finstad, E. P. Lozowski, and L. Makkonen, On the median volume diameter approximation for droplet collision efficiency, *J. Atmos. Sci.* **45**, 4008 (1988).
- [20] C. Phillips and S. Kaye, The influence of the viscous boundary layer on the critical Stokes number for particle impaction near a stagnation point, *J. Aerosol Sci.* **30**, 709 (1999).
- [21] A. D. Araújo, J. S. Andrade, and H. J. Herrmann, Critical role of gravity in filters, *Phys. Rev. Lett.* **97**, 138001 (2006).
- [22] R. Vallée, C. Henry, E. Hachem, and J. Bec, Inelastic accretion of inertial particles by a towed sphere, *Phys. Rev. Fluids* **3**, 024303 (2018).
- [23] M. R. Turner and R. P. Sear, Critical scaling law for the deposition efficiency of inertia-driven particle collisions with a cylinder in high Reynolds number air flow, *Phys. Rev. Fluids* **8**, 014302 (2023).
- [24] D. J. Acheson, *Elementary Fluid Dynamics* (Clarendon Press, Oxford, UK, 1990).
- [25] J. B. Wong, W. E. Ranz, and H. F. Johnstone, Inertial impaction

- of aerosol particles on cylinders, *J. Appl. Phys.* **26**, 244 (1955).
- [26] L. Makkonen and J. Stallabrass, Experiments on the cloud droplet collision efficiency of cylinders, *J. Appl. Meteorol. Clim.* **26**, 1406 (1987); L. Makkonen, Analysis of rotating multicylinder data in measuring cloud-droplet size and liquid water content, *J. Atmos. Ocean. Technol.* **9**, 258 (1992); L. Makkonen, J. Zhang, T. Karlsson, and M. Tiihonen, Modelling the growth of large rime ice accretions, *Cold Reg. Sci. Technol.* **151**, 133 (2018).
- [27] J. F. Robinson, P. B. Warren, and R. P. Sear, *rimeflows: calculations of particle deposition by various flows*, <https://github.com/tranqui/rimeflows> (2025).
- [28] J. Fernandez de la Mora and D. E. Rosner, Effects of inertia on the diffusional deposition of small particles to spheres and cylinders at low Reynolds numbers, *J. Fluid Mech.* **125**, 379 (1982).
- [29] This situation is analogous to how the Reynolds number varies with length scale in classical problems considering the flow past an object (e.g. sphere or cylinder). These singular problems prompted the development of asymptotic techniques. See e.g. Ref. [36] for discussion and historical context.
- [30] This misleadingly-named phenomenon is not truly a paradox. See [36] for a comprehensive discussion and historical account.
- [31] M. Van Dyke, *Perturbation Methods in Fluid Mechanics* (Parabolic Press, Stanford, CA, 1975).
- [32] S. Kuwabara, The forces experienced by randomly distributed parallel circular cylinders or spheres in a viscous flow at small Reynolds numbers, *J. Phys. Soc. Japan* **14**, 527 (1959).
- [33] In the inviscid case, $St_c = 1/4$ is an upper bound. If the initial speed \dot{x} is made large enough, then a critical Stokes number dependent on initial conditions is obtained, just as in the Stokes-flow case. However, our studies with global flow fields always found $St_c = 1/4$.
- [34] K. Hiemenz, Die Grenzschicht an einem in den gleichförmigen Flüssigkeitsstrom eingetauchten geraden Kreiszyylinder, *Dinglers Polytech. J.* **326**, 321 (1911).
- [35] H. Schlichting and K. Gersten, *Boundary-Layer Theory* (Springer-Verlag, Heidelberg, Germany, 2017).
- [36] J. Veysey and N. Goldenfeld, Simple viscous flows: From boundary layers to the renormalization group, *Rev. Mod. Phys.* **79**, 883 (2007).
- [37] J. F. Robinson and P. B. Warren, Renormalisation group theory applied to $\ddot{x} + \dot{x} + x^2 = 0$ (2024), arXiv: 2412.16578.
- [38] L.-Y. Chen, N. Goldenfeld, Y. Oono, and G. Paquette, Selection, stability and renormalization, *Physica A* **204**, 111 (1994); L.-Y. Chen, N. Goldenfeld, and Y. Oono, Renormalization group and singular perturbations: Multiple scales, boundary layers, and reductive perturbation theory, *Phys. Rev. E* **54**, 376 (1996); E. Kirkinis, Secular series and renormalization group for amplitude equations, *Phys. Rev. E* **78**, 032104 (2008).
- [39] L. Gao, T. Tao, Y. Liu, and H. Hu, A field study of ice accretion and its effects on the power production of utility-scale wind turbines, *Renew. Energ.* **167**, 917 (2021).
- [40] L. J. Clancy, *Aerodynamics* (Pitman Publishing Limited, London, UK, 1975).